ACS NANO

Open Access

www.acsnano.org

ARTICLE

Interfacial Distortion of Sb_2Te_3–Sb_2Se_3 Multilayers via Atomic Layer Deposition for Enhanced Thermoelectric Properties

Jun Yang, Mohammadreza Daqiqshirazi, Tobias Ritschel, Amin Bahrami, Sebastian Lehmann, Daniel Wolf, Wen Feng, Almut Pöhl, Jaroslav Charvot, Filip Bureš, Thomas Brumme, Axel Lubk, Jochen Geck, and Kornelius Nielsch*

Cite This: *ACS Nano* 2024, 18, 17500–17508

Read Online

ACCESS | Metrics & More | Article Recommendations | Supporting Information

ABSTRACT: **Atomic layer deposition (ALD) is an effective technique for depositing thin films with precise control of layer thickness and functional properties. In this work, Sb_2Te_3–Sb_2Se_3 nanostructures were synthesized using thermal ALD. A decrease in the Sb_2Te_3 layer thickness led to the emergence of distinct peaks from the Laue rings, indicative of a highly textured film structure with optimized crystallinity. Density functional theory simulations revealed that carrier redistribution occurs at the interface to establish charge equilibrium. By carefully optimizing the layer thicknesses, we achieved an obvious enhancement in the Seebeck coefficient, reaching a peak figure of merit (zT) value of 0.38 at room temperature. These investigations not only provide strong evidence for the potential of ALD manipulation to improve the electrical performance of metal chalcogenides but also offer valuable insights into achieving high performance in two-dimensional materials.**

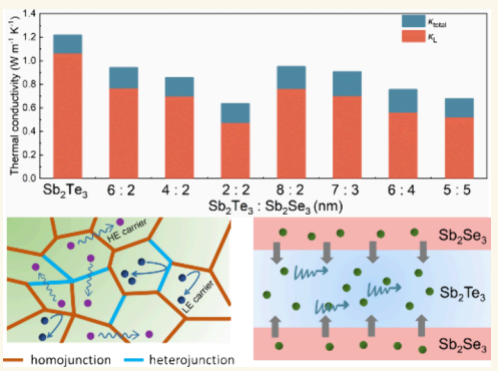

KEYWORDS: *atomic layer deposition, Sb_2Te_3–Sb_2Se_3, 2D materials, interface engineering, transport property*

1. INTRODUCTION

Thermoelectric (TE) materials have the capacity to directly convert heat energy into electrical power, rendering them highly promising for microenergy harvesting applications in Internet of Things devices.[1] The heat-to-electricity conversion efficiency of thermoelectric materials can be evaluated by the dimensionless figure of merit (zT), which is defined as $zT = \sigma S^2 T/\kappa$, where σ, S, T, and κ are the electrical conductivity, Seebeck coefficient, absolute temperature, and total thermal conductivity, respectively. κ is a combination of electronic (κ_E) and lattice (κ_L) thermal conductivities. Enhancing the TE power factor (σS^2) in any material necessitates precise control of the critical transport parameters. A high power factor in thermoelectric materials indicates their efficient conversion of a temperature difference into electrical power.[2] This efficiency enhancement results in increased power output, enhanced energy conversion efficiency, reduced energy losses, and optimal power transfer, making high power factor thermoelectric materials highly sought after for various applications. However, these thermoelectric parameters are intrinsically intertwined, posing a significant hurdle in their independent optimization.

One of the effective strategies to enhance thermoelectric performance is to reduce the dimensions, thereby introducing the quantum confinement effect in nanostructured thermoelectric materials.[3] The electronic states are confined by closed geometries at the nanometer scale, leading to quantized energy levels and enhancing the density of electron states per unit volume occurring for a small well within.[4] In this case, the carrier effective mass and Seebeck coefficient can be elevated rapidly. Hicks et al. demonstrated a 3-fold increase in the Seebeck coefficient value of PbTe/$Pb_{0.927}Eu_{0.073}Te$ compared to bulk PbTe, attributed to the quantum confinement effect in the nanostructured system.[5] As an alternative, Gao et al. fabricated PbSe/SnSe multiple quantum well structures, achieving a high power factor of 25.7 $\mu W\ cm^{-1}\ K^{-2}$ at 300 K, which is 4 times larger than that of a PbSe single layer.[6]

Received: December 28, 2023
Revised: June 17, 2024
Accepted: June 18, 2024
Published: June 26, 2024

https://doi.org/10.1021/acsnano.3c13152
ACS Nano 2024, 18, 17500–17508

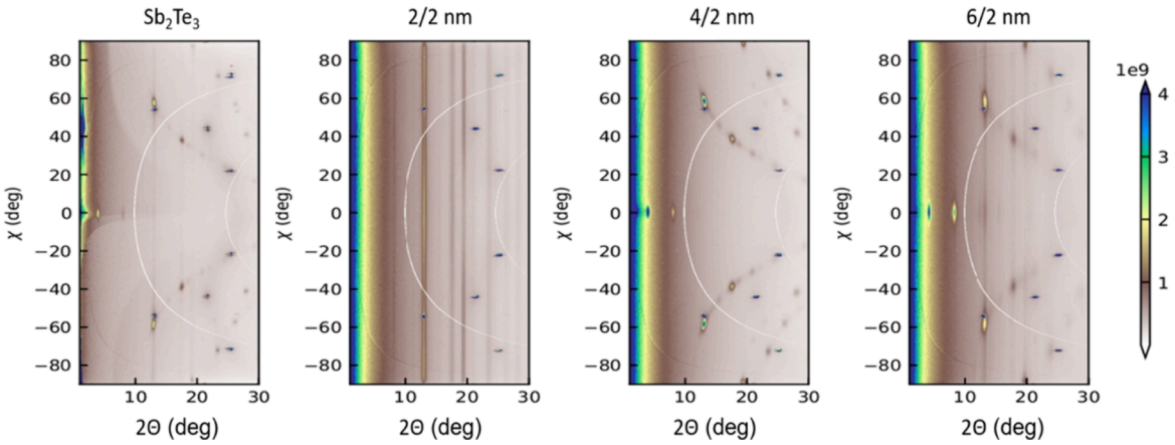

Figure 1. Regrouped scattered X-ray intensity as a function of scattering angle 2θ and polar angle χ, i.e., angle along the Laue cone for the samples Sb_2Te_3 and with Sb_2Te_3:Sb_2Se_3 ratios of 2:2, 4:2, and 6:2 (nm).

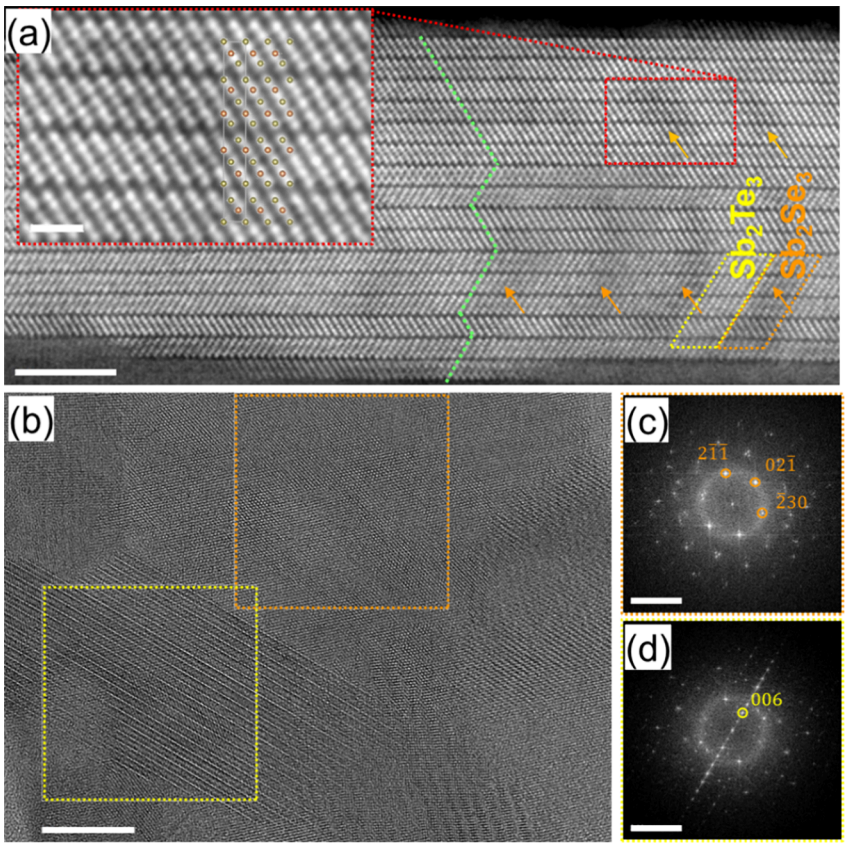

Figure 2. Structural characterizations of Sb_2Te_3−Sb_2Se_3 thin films. (a) HAADF-STEM image of a Sb_2Te_3−Sb_2Se_3 multilayer grain taken along its [010] zone-axis orientation and *c* axis in the vertical direction (scale bar: 5 nm). The inset shows a zoom-in of the region marked by the red dashed box, in which the atomic Sb_2Te_3 model is overlaid (scale bar: 1 nm). The orange arrows highlight the Sb_2Se_3 regions, which appear slightly darker in the image due to their lower Z-contrast. (b) HRTEM images show different grains of the poly crystalline structure (scale bar: 10 nm). (c, d) Fourier transforms (FTs) of regions marked by orange (c) and yellow (d) dashed boxes in panel (b) (scale bars: 5 nm^{-1}). (c) FT shows reflections corresponding to the [324] orientation of the orthorhombic phase with a *Pbnm* space group. (d) The FT shows, e.g., the 006 reflection, indicating a direction parallel to the *c* axis of the $R\bar{3}m$ space group.

Mune et al. implemented a $SrTi_{0.8}Nb_{0.2}O_3$ (conductor) layer between $SrTiO_3$ (insulator) films, resulting in an improved Seebeck coefficient from 61 to 320 $\mu V\ K^{-1}$.[7] However, as the insulator barrier does not contribute to electronic transportation, there was no improvement in the carrier concentration and electrical conductivity.

In addition to high *S*, κ is also a crucial parameter in determining the thermoelectric performance of a material. Ren and Dow demonstrated that the thermal conductivities of multilayer thin films are lower than those of their corresponding bulk materials, employing the classical Boltzmann transport equation approach with a quantum mechanical treatment of the scattering rate.[8] The presence of high-density superlattice interfaces leads to strong phonon scattering, resulting in a significant reduction in lattice thermal conductivity. The Bi_2Te_3 (1 nm)/Sb_2Te_3 (5 nm) superlattice

https://doi.org/10.1021/acsnano.3c13152
ACS Nano 2024, 18, 17500−17508

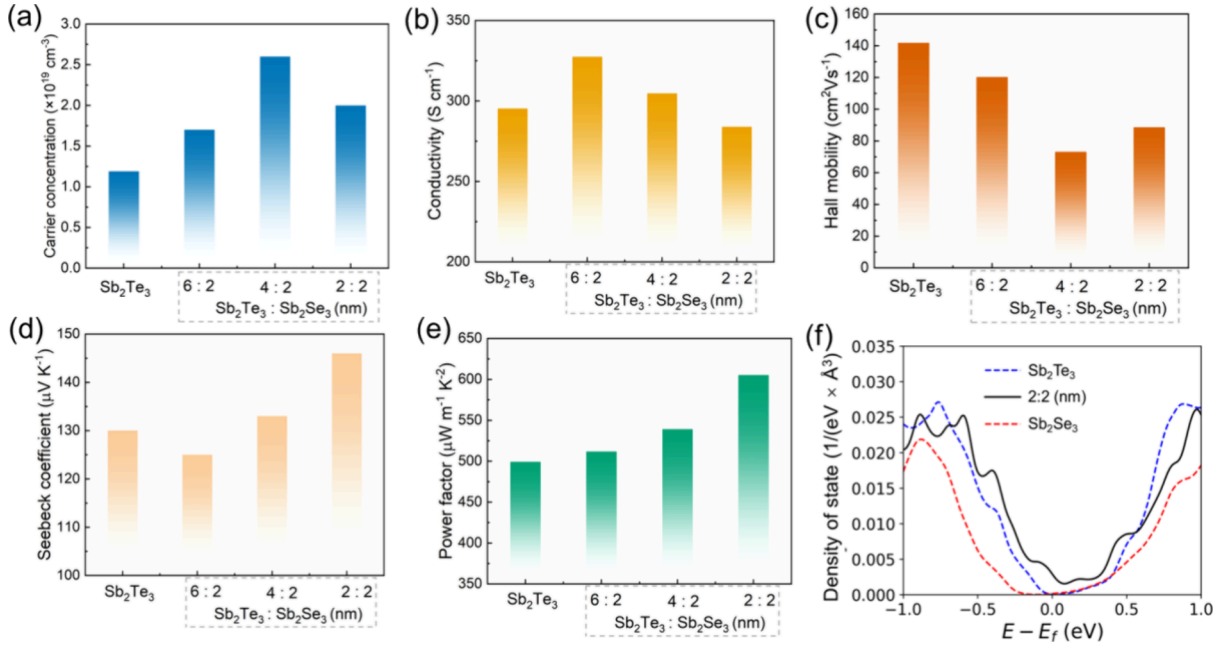

Figure 3. Transport properties of Sb_2Te_3−Sb_2Se_3 nanostructured films: (a) carrier concentration, (b) electrical conductivity, (c) mobility, and (d) Seebeck coefficient. (e) Power factor of thin films. (f) Density of states (DOS) for the three bulk systems of Sb_2Te_3, Sb_2Se_3, and Sb_2Te_3−Sb_2Se_3 films.

structure constructed by Winkler yielded an ultralow lattice thermal conductivity of 0.23 W m^{-1} K^{-1}.[9] Tang and colleagues recently fabricated the $MoTe_2/Bi_2Te_3$ system. The interfacial scattering of phonons has resulted in a notable reduction of κ_L, with values in the produced superlattice films ranging from 0.31 to 0.39 W m^{-1} K^{-1}.[10] In addition, several factors that contribute to reducing thermal conductivity, including lattice mismatch at the interfaces, alloy scattering, phonon minigap formation, and phonon tunneling, have been investigated with the aim of optimizing thermal conductivity in superlattices.[11−13]

While artificially engineered thermoelectric nanostructures hold great promise for synergistically optimizing transport parameters, the rational design, reliable fabrication, and the mechanism responsible for optimizing electrical properties remain elusive and pose significant challenges. Here, nanostructured thin films of Sb_2Te_3−Sb_2Se_3 were successfully synthesized using thermal ALD,[14] with the composition of this nanostructure precisely controlled by adjusting the ALD cycle numbers for Sb_2Te_3 and Sb_2Se_3. A systematic study of the crystal structures and transport properties revealed an obvious improvement in the thermoelectric performance upon careful optimization of the Sb_2Se_3 sublayer thickness. The sample Sb_2Te_3:Sb_2Se_3 = 5:5 (nm) exhibited an impressive Seebeck coefficient of 174 μV K^{-1} at room temperature. Further investigation demonstrated a high power factor of 852 μW m^{-1} K^{-2} accompanied by a peak zT value of 0.38 at room temperature.

2. RESULTS AND DISCUSSION

Before the structures were synthesized, the growth behaviors of single-phase Sb_2Te_3 and Sb_2Se_3 films were investigated. For Sb_2Te_3 films, a combination of $SbCl_3$ and $(Et_3Si)_2Te$ precursors was employed, whereas for Sb_2Se_3 films, $SbCl_3$ and $Se(SnMe_3)_2$ precursors were utilized.[15,16] The Sb_2Te_3 and Sb_2Se_3 thin films were grown at 80 and 110 °C without any vacuum break, respectively (see more details in the Experimental Section). The structural characterizations of Sb_2Te_3−Sb_2Se_3 are shown in Figure 1 and Figure S1 in the Supporting Information. Grazing incidence X-ray diffraction (GID) measurements were performed using a custom-built laboratory setup equipped with a Mo Kα source to analyze the structural characteristics of the samples. The corresponding data reveals that Sb_2Te_3 exhibits a rhombohedral phase with a space group of $R\bar{3}m$, while Sb_2Se_3 adopts an orthorhombic phase with a *Pbnm* space group. As the thickness of the Sb_2Te_3 layer decreases, distinctive peaks emerge from the Laue rings, signifying a highly textured film structure achieving optimal crystallinity in the sample Sb_2Te_3:Sb_2Se_3 = 4:2 (nm). On the other hand, the sample Sb_2Te_3:Sb_2Se_3 = 2:2 (nm) has a lower diffraction intensity than the other samples, suggesting a smaller grain size.

To investigate the microstructure of the Sb_2Te_3−Sb_2Se_3 nanocomposites, cross-sectional imaging at atomic resolution was performed using high-resolution transmission electron microscopy in both bright-field mode (HRTEM) and high-angle annular dark-field scanning mode (HAADF-STEM). A representative HAADF-STEM image of a single grain taken along [010] zone-axis orientation according to the rhombohedral Sb_2Te_3 crystal structure is shown in Figure 2a. The latter reveals an atomic zigzag arrangement between the mono-, bi-, and multilayers highlighted by a green dashed line indicating the existence of twin boundaries.[17] Furthermore, a faint bright-dark atomic (Z-) contrast modulation is visible with a periodicity in the horizontal direction of about 2 nm in which the Te atoms appear brighter (Z = 52) than the Se atoms (Z = 34). In fact, this coincides with the intended alternation between Sb_2Te_3 and Sb_2Se_3 deposition, where in this case the Sb_2Se_3 adopts the $R\bar{3}m$ crystal structure of the Sb_2Te_3. This observation is also confirmed by STEM energy-dispersive X-ray mapping (STEM-EDX), as illustrated in Figure S2 of the Supporting Information. It should be noted

https://doi.org/10.1021/acsnano.3c13152
ACS Nano 2024, 18, 17500−17508

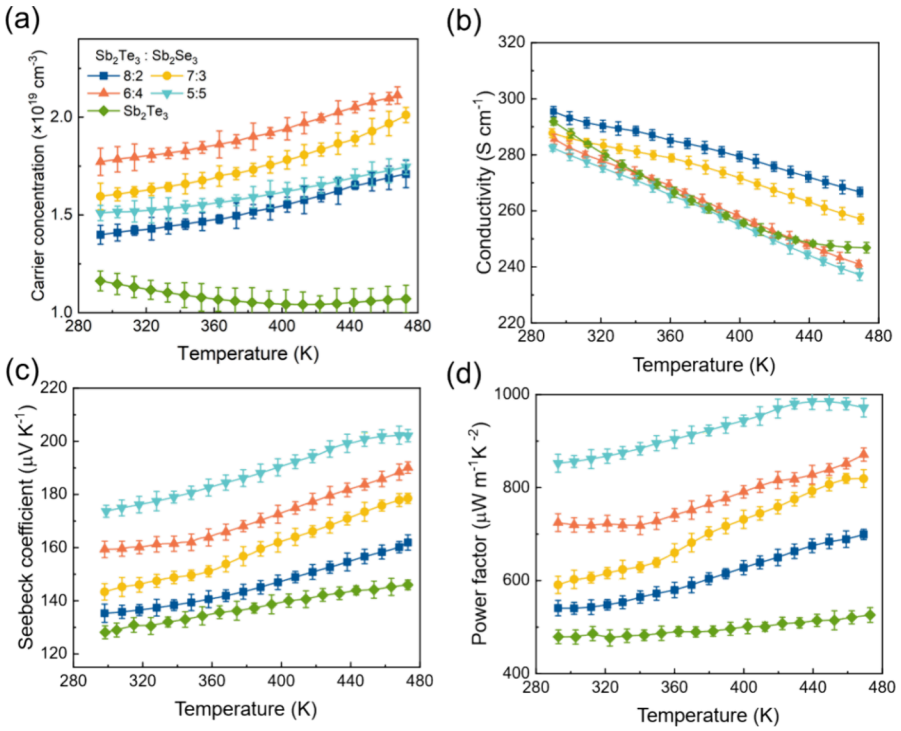

Figure 4. Temperature-dependent electrical transport properties of Sb_2Te_3−Sb_2Se_3 thin films: (a) carrier concentration, (b) conductivity, (c) Seebeck coefficient, and (d) power factor.

that ALD growth at relatively low temperatures leads to polycrystalline layers. For low-cycle ALD of Sb_2Te_3, the presence of dangling bonds at the layer edges preferentially adsorbs precursor molecules.[18] This phenomenon may diverge from the conventional monolayer-by-monolayer arrangement, instead leading to the formation of an expanding alloy cluster (Volmer−Weber growth behavior).[18,19] Furthermore, the exchange reaction at the gas−solid interface during the ALD can contribute to alloying. The exposure of the Se precursor onto the Sb_2Te_3 surface leads to the exchange of Se by Te atoms at the interface, resulting in the formation of alloy clusters and atomic-scale distortions.[20] For example, the HRTEM image in Figure 2b depicts different grains, two of which are marked with dashed squares in yellow and orange. The corresponding Fourier transforms (FTs) of these marked regions displayed in Figure 2c,d are consistent with two different structures. The FT of the upper grain (Figure 2c) shows reflections corresponding to the [324] orientation of the orthorhombic phase with a *Pbnm* space group, whereas the FT of the lower grain (Figure 2d) reveals, e.g., the 006 reflection, indicating a direction parallel to the *c* axis of the $R\bar{3}m$ space group. The incorporation of dopants into the pristine layered films has been observed to improve the Seebeck coefficient, which will be discussed in the following sections.

Figure 3 depicts the room temperature electrical transport properties of the Sb_2Te_3−Sb_2Se_3 structures. The carrier concentration of the Sb_2Te_3 thin film is 1.18×10^{19} cm^{-3} and reaches a peak value of 2.61×10^{19} cm^{-3} in the Sb_2Te_3:Sb_2Se_3 = 4:2 (nm) structure. The carrier concentration of Sb_2Se_3 is 3.6×10^{18} cm^{-3} at room temperature. Considering the bandgaps for Sb_2Te_3 and Sb_2Se_3 as 0.3 and 1.14 eV, respectively, a band offset occurs for the Sb_2Te_3−Sb_2Se_3 heterostructure.[21−23] The significantly higher work function difference between Sb_2Se_3 and Sb_2Te_3 results in a pronounced hole junction from Sb_2Se_3 to Sb_2Te_3.[6,24] The thicker Sb_2Te_3 layer in the structure facilitates a larger potential drop at the Sb_2Te_3/Sb_2Se_3 interface, leading to a higher carrier concentration compared to a thinner Sb_2Te_3 layer.[6] However, a slight decrease in the carrier concentration is observed when the Sb_2Te_3 to Sb_2Se_3 ratio is further reduced. Specifically, the carrier concentration of the Sb_2Te_3:Sb_2Se_3 = 2:2 (nm) sample is lower than that of Sb_2Te_3:Sb_2Se_3 = 4:2 (nm). In the Sb_2Te_3:Sb_2Se_3 = 2:2 (nm) sample, the Sb_2Te_3 layer is too thin to effectively shield the built-in potential, resulting in carrier pinning at the interface.[6] Under these conditions, charge transfer occurs more readily in Sb_2Se_3 with a thicker Sb_2Te_3 layer, leading to a higher carrier concentration. The highest electrical conductivity of 327 S cm^{-1} was achieved at Sb_2Te_3:Sb_2Se_3 = 6:2 (nm) (Figure 3b). The Hall mobility of the systems falls within the range of 90−120 cm^2 V^{-1} s^{-1}, which is lower than a value of 140 cm^2 V^{-1} s^{-1} observed in the Sb_2Te_3 layer (Figure 3c). Interface scattering arises when carriers traverse between different layers, leading to mobility restrictions and impacting overall mobility.[25] Additionally, potential barriers within the superlattice structure can obstruct the interlayer transport of charge carriers, further reducing mobility.[26] Furthermore, interface effects can induce the formation of interface states, which act as scattering centers for carriers, contributing to additional charge scattering and a subsequent decrease in mobility.[27] Conversely, an inverse trend is evident in the Seebeck coefficient results. For instance, as depicted in Figure 3d, the lowest Seebeck coefficient of 125 μV K^{-1} is obtained at Sb_2Te_3:Sb_2Se_3 = 6:2 (nm), while the Sb_2Te_3:Sb_2Se_3 = 2:2 (nm) sample exhibits the highest value of 146 μV K^{-1}. The room temperature transport properties correspond well with the theoretical calculation results based on replacement modes, which can be supported by density functional theory results in Table S2 and Figures S3 and S4 in

https://doi.org/10.1021/acsnano.3c13152
ACS Nano 2024, 18, 17500−17508

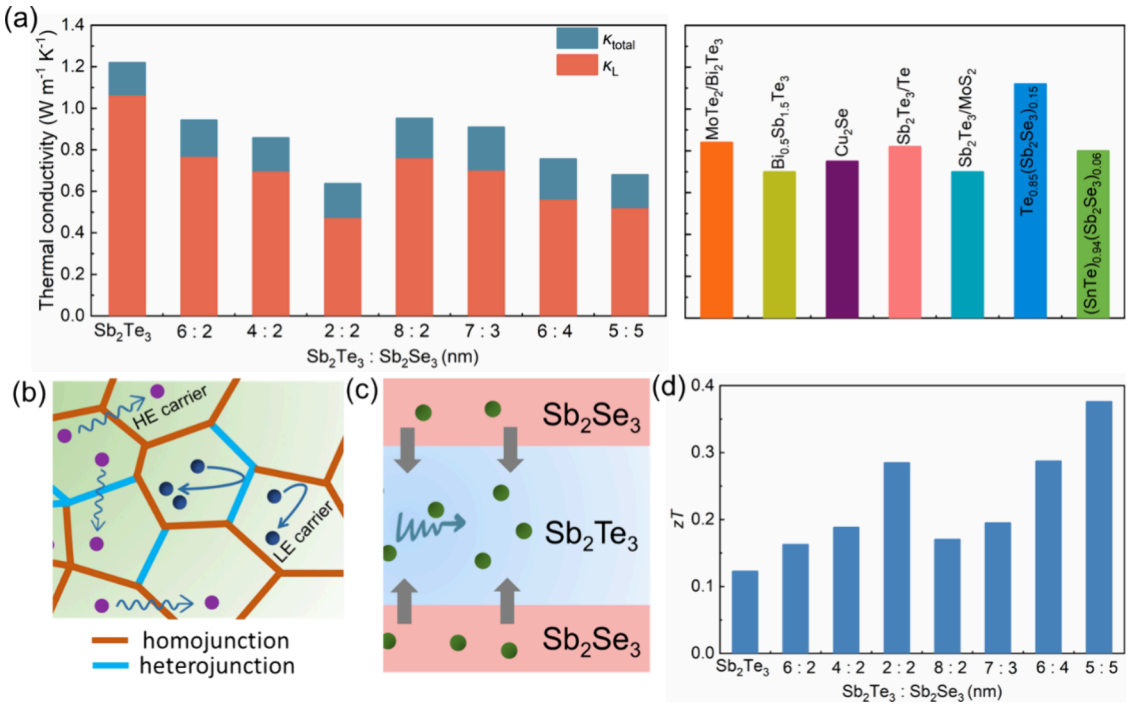

Figure 5. (a) Total thermal conductivity and lattice thermal conductivity of Sb_2Te_3−Sb_2Se_3 thin films and the comparison with reported data at room temperature.[10,31−37] The models of (b) alloy and (c) superlattice structures in the thin films. (d) zT values for various samples at room temperature.

the Supporting Information. The bandgap is minimally affected by the strain induced by the lattice mismatch between Sb_2Te_3 and Sb_2Se_3. Instead, it is the states far from the Fermi energy that are primarily influenced. The strain can alter the thermoelectric coefficient slightly due to the changes in the electronic states. Further discussion on lattice mismatch can be found in the Supporting Information (Table S3 and Figure S5).

The single parabolic band (SPB) model is the most widely employed approach for evaluating the electrical transport properties of thermoelectric materials.[28,29] The relationship between the Seebeck coefficient and carrier concentration at room temperature was determined using the Pisarenko plot, as shown in Figure S6 in the Supporting Information. The effective mass (m^*) increases from 0.38m_e to 0.65m_e with the rising doping level of Sb_2Se_3 into the Sb_2Te_3 system. Notably, the m^* of the Sb_2Te_3−Sb_2Se_3 layer is significantly higher than that of the Sb_2Te_3 layer, indicating the presence of band bending and the energy filtering effect in the heterostructure system. Additionally, the incorporation of the quantum confinement effect in the multilayer system further enhances m^*, given that the thickness is smaller than the de Broglie wavelength of electrons.[30] The power factor was calculated using the electrical conductivity and Seebeck coefficient data (Figure 3e). A maximum PF value of 605 μW m^{-1} K^{-2} was determined for the sample Sb_2Te_3:Sb_2Se_3 = 2:2 (nm) at room temperature, primarily attributed to the high Seebeck coefficient. The sample Sb_2Te_3:Sb_2Se_3 = 2:2 (nm) appears more semimetallic, as indicated by the DOS not approaching zero in the bandgap region (Figure 3f). Moreover, a slight decrease in the bandgap is observed, accompanied by a slight shift and enhancement of the Fermi level, contributing to the improved Seebeck coefficient.

To investigate the electrical properties of Sb_2Te_3−Sb_2Se_3 nanostructures while minimizing the influence on their alloyed structure, samples with higher thickness ratios were fabricated. The temperature-dependent carrier concentration, conductivity, and Seebeck coefficient were explored, as displayed in Figure 4. The Sb_2Te_3−Sb_2Se_3 samples exhibit distinct transport behavior compared to the Sb_2Te_3 layer. At room temperature, the highest n of 1.78 × 10^{19} cm^{-3} was achieved for the sample Sb_2Te_3:Sb_2Se_3 = 6:4 (nm). The electrical conductivity of Sb_2Te_3−Sb_2Se_3 structures showed minimal variation compared to the Sb_2Te_3 single layer. The highest σ of 295.45 S cm^{-1} was achieved for the Sb_2Te_3:Sb_2Se_3 = 8:2 (nm) sample, closely followed by the value of 291.23 S cm^{-1} for Sb_2Te_3. All thin films exhibited positive S values, confirming their p-type semiconducting nature. A Seebeck coefficient of 174 μV K^{-1} was obtained at room temperature, representing a 35% enhancement compared to the Sb_2Te_3 layer. This significant increase in the Seebeck coefficient for the Sb_2Te_3−Sb_2Se_3 superlattice layers resulted in an exceptional power factor reaching up to 852 μW m^{-1} K^{-2} at room temperature.

The thermal conductivity of Sb_2Te_3−Sb_2Se_3 films was evaluated at room temperature using the 3-ω technique (Figure 5a). At room temperature, the Sb_2Te_3−Sb_2Se_3 layers exhibited a lower total thermal conductivity (κ_{Total}) compared to pure Sb_2Te_3 layers. The sample with a composition ratio of Sb_2Te_3:Sb_2Se_3 = 2:2 (nm) demonstrated an impressive minimum thermal conductivity of 0.62 W m^{-1} K^{-1}, which is almost 2 times lower than the total thermal conductivity of Sb_2Te_3 (1.23 W m^{-1} K^{-1}). The obtained thermal conductivity is comparable to that of multilayered structures such as Sb_2Te_3−MoS_2 but lower than alloys like $Te_{0.85}(Sb_2Se_3)_{0.06}$ or bulk Sb_2Te_3 or Sb_2Se_3 (Table S4 in the Supporting Information), indicating the significant effectiveness of the

https://doi.org/10.1021/acsnano.3c13152
ACS Nano 2024, 18, 17500−17508

alloyed structure and multilayer period in reducing thermal conductivity.[10,31−37]

According to Wiedemann−Franz law, the electronic (κ_E) and lattice (κ_L) thermal conductivities can be carried out by the following formulas:

$$\kappa_E = L\sigma T \quad (1)$$

$$L = 1.5 + \exp\left[\frac{|S|}{116}\right] \quad (2)$$

$$\kappa_{Total} = \kappa_L + \kappa_E \quad (3)$$

where L is the Lorenz number, T is the temperature, and S is the Seebeck coefficient. The calculated κ_L is also shown in Figure 5a. In the Sb_2Te_3−Sb_2Se_3 system, lattice thermal conductivity primarily contributes to the total thermal conductivity. Generally, increasing the interface density of thin films decreases κ_L, which adequately explains the overall change trend of κ_L.[10] Interestingly, the lattice thermal conductivity of the sample with a composition ratio of Sb_2Te_3:Sb_2Se_3 = 2:2 (nm) (0.46 W m^{-1} K^{-1}) is lower than that of the sample with a composition ratio of Sb_2Te_3:Sb_2Se_3 = 5:5 (nm) (0.51 W m^{-1} K^{-1}), suggesting that additional scattering occurs in the former system. This should be attributed to the different weightings of phonon scattering mechanisms in alloyed structures and quantum confinement effects in superlattice structures, resulting in distinct impacts on thermal conductivity. In systems where the average mean free path of phonons exceeds the limiting dimension of the sample, heat transport does not follow Fourier's law, exhibiting semiballistic phonon transport characteristics.[38,39] This regime highlights the wave nature inherent in phonons, with the potential to sustain coherence and consequently reduce the κ.[40] Low-dimensional nanostructures exhibit favorable TE performance due to quantum confinement effects.[41,42] For the Sb_2Te_3:Sb_2Se_3 = 2:2 (nm) sample, the Volmer−Weber growth mode results in the formation of structural features such as alloy compositions, point defects, or phase boundaries as well as superlattice structures. These structural characteristics collectively contribute to enhanced phonon scattering, consequently reducing the thermal conductivity (Figure 5b,c). In comparison, the Sb_2Te_3:Sb_2Se_3 = 5:5 (nm) sample exhibits a more ordered structure, and the quantum confinement effect is the primary factor responsible for decreasing the thermal conductivity. The rational design of the work function difference will lead to facilitate directional hole injection into the coherent region through modulation doping. To establish charge equilibrium at the interface, carrier redistribution takes place, leading to band bending. Our theoretical simulations provided strong confirmation of the results (see Tables S5−S7 in the Supporting Information). Phonons with mid- to long-wavelengths scattering are enhanced at the heterojunction interfaces, which is considerably more efficient than scattering at normal grain boundaries.[22,26,43] Consequently, the m^* increases and the thermal conductivity decreases simultaneously, leading to a high zT value of 0.38 for the sample Sb_2Te_3:Sb_2Se_3 = 5:5 (nm).

3. CONCLUSIONS

In conclusion, we designed Sb_2Te_3−Sb_2Se_3 nanostructured thin films by using thermal ALD. The transport properties, including the carrier concentration, electrical conductivity, Seebeck coefficient, and thermal conductivity, were evaluated. In the Sb_2Te_3:Sb_2Se_3 = 2:2 (nm) system, Volmer−Weber growth introduced alloy and defect structures that reduce the carrier concentration and Hall mobility. Through meticulous optimization of the sublayer thickness of Sb_2Se_3, a notable improvement was achieved with a high Seebeck coefficient of 174 μV K^{-1}, demonstrating a 35% enhancement compared to the pure Sb_2Te_3 layer. As a result of the increase in S and σ for the Sb_2Te_3−Sb_2Se_3 systems, a high power factor reaches up to 852 μW m^{-1} K^{-2} for the sample Sb_2Te_3:Sb_2Se_3 = 5:5 (nm). The results indicated that the relative contributions of phonon scattering mechanisms and quantum confinement effects could significantly influence the overall thermoelectric performance of nanostructured thin films. This study provides valuable insights into the design and fabrication of high-performance chalcogenides via the ALD technique.

4. EXPERIMENTAL SECTION

Fabrication of Sb_2Te_3 and Sb_2Se_3 Thin Films. The Sb_2Te_3 and Sb_2Se_3 thin films were grown using a thermal ALD reactor (Veeco Savannah S100) at 80 and 110 °C, respectively. $SbCl_3$ and $(Et_3Si)_2Te$ were used for Sb_2Te_3 films, while $Se(SnMe_3)_2$ and $SbCl_3$ were used for Sb_2Se_3 synthesis. During the ALD process, the $SbCl_3$, $(Et_3Si)_2Te$, and $Se(SnMe_3)_2$ were kept at 60, 77, and 60 °C, respectively. High-purity N_2 was used as the carrier gas, and the chamber was kept at a flow rate of 10 sccm during the reaction process. The optimized pulse and purge times for one ALD deposition (precursor 1/N_2/precursor 2/N_2) were 1/10/1/10 s. The detailed ALD process is shown in Table S1 (Supporting Information). The sample identifier Sb_2Te_3:Sb_2Se_3 = 2:2 (nm) indicates that the individual thicknesses of Sb_2Te_3 and Sb_2Se_3 are both 2 nm. The total thickness for all samples is approximately 100 nm.

Characterization of Morphology, Electrical, and Thermal Properties. The thickness of thin films was measured using X-ray reflectometry (X'Pert MRD PRO). Gracing incident X-ray diffraction (GID) was performed using a custom-made laboratory setup with a Mo Kα source (λ = 0.713 Å). We aligned the surface of the films at an angle of 0.5° with respect to the incident X-ray beam. The samples were then rotated about their surface normal, and diffraction images for scattering angles up to 40° were recorded using a 2D pixel detector. The detector images were transformed into reciprocal space, and the diffracted intensity was regrouped into the scattering angle (2θ) and the polar angle along the Laue circles (X) using the pyFAI package.[44] The morphology and atomic structure of thin films were characterized by transmission electron microscopy using a double-corrected (aberration correction in scanning and bright-field mode) ThermoFisher Titan 80-300 operated at a 300 kV acceleration voltage. Thin films were deposited on SiO_2 and Si_3N_4 substrates (TFA chip from Linseis company) for structural characterization and transport property measurements, respectively.[45,46] The detailed platform measurement can be found in the Supporting Information.

Theoretical Calculations. The initial structures were created using the fully relaxed Sb_2Te_3 bulk structure. Sb_2Te_3 consists of three rhombohedral stacked layers each consisting of five atomic layers with a space group of $R\bar{3}m$. The heterostructure systems were made by replacing the Te with Se within one layer to form different mixing ratios of Sb_2Te_3/Sb_2Se_3 layers. Later, the effect of precursor mixing was also studied by Se−Te substitutions within one layer in the 2:2 nm system (Table S2, Supporting Information). Additionally, we also investigated Se_{Te} defects by replacing a single Te atom with Se. For creating various concentrations, 1 × 1 × 1, 2 × 2 × 1, and 3 × 3 × 1 supercells of the hexagonal unit cell were considered. The structures were relaxed until the forces were below 1 meV/Å. The electronic structures were obtained using density functional theory (DFT) with the Perdew−Burke−Ernzerhof (PBE)[47] exchange-correlation functional as implemented in FHI-aims.[48] It is well known that hybrid functionals such as HSE06 can lead to an opening of the bandgap,[49] correcting (sometimes "over"-correcting) the underestimation by (semi)local functionals. On the other hand, the purpose of this study

https://doi.org/10.1021/acsnano.3c13152
ACS Nano 2024, 18, 17500−17508

is to understand the effects of structures and interface variations on the thermoelectric coefficients. It has been shown that (semi)local functionals such as PBE can produce satisfactory results.[50,51] Scalar relativistic corrections (ZORA), spin−orbit coupling (SOC) effects, and nonlocal many-body dispersions were included in the computations as described in the references.[52,53] Subsequently, transport coefficients were calculated based on the Boltzmann transport equation within the constant−relaxation−time approximation employing BoltzTrap2.[54]

ASSOCIATED CONTENT

Supporting Information

The Supporting Information is available free of charge at https://pubs.acs.org/doi/10.1021/acsnano.3c13152.

Additional characterizations such as out-of-plane XRD patterns; EDS mapping for elemental distribution; detailed DFT simulations of defect models, lattice mismatch, and interfacial charge transfer; and transport property measurement platform (PDF)

AUTHOR INFORMATION

Corresponding Author

Kornelius Nielsch − *Leibniz Institute for Solid State and Materials Research, Dresden 01069, Germany; Institute of Materials Science, Technische Universität Dresden, Dresden 01062, Germany;* orcid.org/0000-0003-2271-7726; Email: k.nielsch@ifw-dresden.de

Authors

Jun Yang − *Leibniz Institute for Solid State and Materials Research, Dresden 01069, Germany; Institute of Materials Science, Technische Universität Dresden, Dresden 01062, Germany;* orcid.org/0000-0002-0596-1279

Mohammadreza Daqiqshirazi − *Chair of Theoretical Chemistry, Technische Universität Dresden, Dresden 01069, Germany*

Tobias Ritschel − *Institute of Solid State and Materials Physics, Technische Universität Dresden, Dresden 01069, Germany*

Amin Bahrami − *Leibniz Institute for Solid State and Materials Research, Dresden 01069, Germany;* orcid.org/0000-0001-8851-7351

Sebastian Lehmann − *Leibniz Institute for Solid State and Materials Research, Dresden 01069, Germany*

Daniel Wolf − *Leibniz Institute for Solid State and Materials Research, Dresden 01069, Germany;* orcid.org/0000-0001-5000-8578

Wen Feng − *Leibniz Institute for Solid State and Materials Research, Dresden 01069, Germany*

Almut Pöhl − *Leibniz Institute for Solid State and Materials Research, Dresden 01069, Germany*

Jaroslav Charvot − *Institute of Organic Chemistry and Technology, Faculty of Chemical Technology, University of Pardubice, Pardubice 53210, Czech Republic*

Filip Bureš − *Institute of Organic Chemistry and Technology, Faculty of Chemical Technology, University of Pardubice, Pardubice 53210, Czech Republic;* orcid.org/0000-0002-2832-6673

Thomas Brumme − *Chair of Theoretical Chemistry, Technische Universität Dresden, Dresden 01069, Germany;* orcid.org/0000-0002-5033-1065

Axel Lubk − *Leibniz Institute for Solid State and Materials Research, Dresden 01069, Germany;* orcid.org/0000-0003-2698-8806

Jochen Geck − *Institute of Solid State and Materials Physics, Technische Universität Dresden, Dresden 01069, Germany*

Complete contact information is available at: https://pubs.acs.org/10.1021/acsnano.3c13152

Notes

The authors declare no competing financial interest.

ACKNOWLEDGMENTS

This work was supported by the Program of Collaborative Research Centers in Germany (grant no. SFB 1415). M.D. and T.B. would like to acknowledge the Gauss Centre for Supercomputing e.V. (www.gauss-centre.eu) for funding (project ID no. 29026) this project by providing computing time through the John von Neumann Institute for Computing (NIC) on the GCS Supercomputer JUWELS[55] at Jülich Supercomputing Centre (JSC).

REFERENCES

(1) Nandihalli, N. Thermoelectric Films and Periodic Structures and Spin Seebeck Effect Systems: Facets of Performance Optimization. *Mater. Today Energy* **2022**, *25*, No. 100965, DOI: 10.1016/j.mtener.2022.100965.

(2) Zheng, Z.-H.; Zhang, D.-L.; Jabar, B.; Chen, T.-B.; Nisar, M.; Chen, Y.-F.; Li, F.; Chen, S.; Liang, G.-X.; Zhang, X.-H.; Fan, P.; Chen, Y.-X. Realizing High Thermoelectric Performance in Highly (0l0)-Textured Flexible Cu2se Thin Film for Wearable Energy Harvesting. *Mater. Today Phys.* **2022**, *24*, No. 100659.

(3) Katan, C.; Mercier, N.; Even, J. Quantum and Dielectric Confinement Effects in Lower-Dimensional Hybrid Perovskite Semiconductors. *Chem. Rev.* **2019**, *119* (5), 3140−3192.

(4) Herrera, E.; Guillamón, I.; Barrena, V.; Herrera, W. J.; Galvis, J. A.; Yeyati, A. L.; Rusz, J.; Oppeneer, P. M.; Knebel, G.; Brison, J. P.; Flouquet, J.; Aoki, D.; Suderow, H. Quantum-Well States at the Surface of a Heavy-Fermion Superconductor. *Nature* **2023**, *616* (7957), 465−469.

(5) Hicks, L. D.; Harman, T. C.; Sun, X.; Dresselhaus, M. S. Experimental Study of the Effect of Quantum-Well Structures on the Thermoelectric Figure of Merit. *Phys. Rev. B* **1996**, *53* (16), R10493.

(6) Gao, Z.; Ning, X.; Wang, J.; Wang, J.; Wang, S. Ultrahigh Power Factor and Ultralow Thermal Conductivity at Room Temperature in Pbse/Snse Superlattice: Role of Quantum-Well Effect. *Small* **2022**, *18* (1), e2104916.

(7) Mune, Y.; Ohta, H.; Koumoto, K.; Mizoguchi, T.; Ikuhara, Y. Enhanced Seebeck Coefficient of Quantum-Confined Electrons in Sr Ti O 3/ Sr Ti 0.8 Nb 0.2 O 3 Superlattices. *Appl. Phys. Lett.* **2007**, *91* (19), No. 192105.

(8) Ren, S. Y.; Dow, J. D. Thermal Conductivity of Superlattices. *Phys. Rev. B* **1982**, *25* (6), 3750.

(9) Winkler, M. *Nanostructured Thermoelectrics: Bi2te3/Sb2te3 Based Superlattice Systems Fabricated by Mbe and Sputtering. Doctoral dissertation,*Universität Tübingen2015.

(10) Zhang, C.; Chen, Z.; Bai, H.; Lin, W.; Yang, M.; Hong, M.; Zhan, F.; Xie, S.; Zhang, M.; Li, Z.; Wang, Z.; Luo, Y.; Yang, J.; Wang, R.; Wu, J.; Zhang, H.; Zhang, Q.; Liu, W.; Tang, X. Manipulating the Interfacial Band Bending for Enhancing the Thermoelectric Properties of 1t'-Mote(2) /Bi(2) Te(3) Superlattice Films. *Small* **2023**, *19*, e2300745.

(11) Spindlberger, A.; Kysylychyn, D.; Thumfart, L.; Adhikari, R.; Rastelli, A.; Bonanni, A. Cross-Plane Thermal Conductivity of Gan/Aln Superlattices. *Appl. Phys. Lett.* **2021**, *118* (6), No. 062105.

(12) Narayanamurti, V.; Störmer, H. L.; Chin, M. A.; Gossard, A. C.; Wiegmann, W. Selective Transmission of High-Frequency Phonons

by a Superlattice: The″ Dielectric″ Phonon Filter. *Phys. Rev. Lett.* **1979**, *43* (27), 2012.
(13) Lee, S. M.; Cahill, D. G.; Venkatasubramanian, R. Thermal Conductivity of Si−Ge Superlattices. *Appl. Phys. Lett.* **1997**, *70* (22), 2957−2959.
(14) Yang, J.; Bahrami, A.; Ding, X. W.; Lehmann, S.; Kruse, N.; He, S. Y.; Wang, B. W.; Hantusch, M.; Nielsch, K. Characteristics of Ald-Zno Thin Film Transistor Using H2o and H2o2 as Oxygen Sources. *Adv. Mater. Interfaces* **2022**, *9* (15), 2101953.
(15) Charvot, J.; Zazpe, R.; Macak, J. M.; Bureš, F. Organoselenium Precursors for Atomic Layer Deposition. *ACS Omega* **2021**, *6* (10), 6554−6558.
(16) Koch, V. M.; Charvot, J.; Cao, Y.; Hartmann, C.; Wilks, R. G.; Kundrata, I.; Mínguez-Bacho, I.; Gheshlaghi, N.; Hoga, F.; Stubhan, T.; Alex, W.; Pokorný, D.; Topraksal, E.; Smith, A.-S.; Brabec, C. J.; Bär, M.; Guldi, D. M.; Barr, M. K. S.; Bureš, F.; Bachmann, J. Sb2se3 Thin-Film Growth by Solution Atomic Layer Deposition. *Chem. Mater.* **2022**, *34* (21), 9392−9401.
(17) Cremer, S.; Voß, L.; Braun, N.; Wolff, N.; Kienle, L.; Lotnyk, A. Growth and Microstructure of Gete-Sb2te3 Heterostructures Prepared by Pulsed Laser Deposition. *Appl. Surf. Sci.* **2024**, *655*, No. 159679.
(18) Sharma, A.; Verheijen, M. A.; Wu, L.; Karwal, S.; Vandalon, V.; Knoops, H. C. M.; Sundaram, R. S.; Hofmann, J. P.; Kessels, W.; Bol, A. A. Low-Temperature Plasma-Enhanced Atomic Layer Deposition of 2-D Mos(2): Large Area. *Thickness Control and Tuneable Morphology. Nanoscale* **2018**, *10* (18), 8615−8627.
(19) Heo, H.; Sung, J. H.; Ahn, J.-H.; Ghahari, F.; Taniguchi, T.; Watanabe, K.; Kim, P.; Jo, M.-H. Frank−Van Der Merwe Growth Versus Volmer−Weber Growth in Successive Stacking of a Few-Layer Bi2te3/Sb2te3 by Van Der Waals Heteroepitaxy: The Critical Roles of Finite Lattice-Mismatch with Seed Substrates. *Adv. Electron. Mater.* **2017**, *3* (2), 1600375 DOI: 10.1002/aelm.201600375.
(20) Wiegand, C. W.; Zierold, R.; Faust, R.; Pohl, D.; Thomas, A.; Rellinghaus, B.; Nielsch, K. Surface Modification of V-Vi Semiconductors Using Exchange Reactions within Ald Half-Cycles. *Adv. Mater. Interfaces* **2018**, *5* (5), 1701155 DOI: 10.1002/admi.201701155.
(21) Yang, J.; Li, J.; Bahrami, A.; Nasiri, N.; Lehmann, S.; Cichocka, M. O.; Mukherjee, S.; Nielsch, K. Wafer-Scale Growth of Sb2te3 Films Via Low-Temperature Atomic Layer Deposition for Self-Powered Photodetectors. *ACS Appl. Mater. Interfaces* **2022**, *14* (48), 54034−54043.
(22) Yang, J.; Mukherjee, S.; Lehmann, S.; Krahl, F.; Wang, X.; Potapov, P.; Lubk, A.; Ritschel, T.; Geck, J.; Nielsch, K. Low-Temperature ALD of SbOx/Sb2Te3 Multilayers with Boosted Thermoelectric Performance. *Small* **2024**, *20* (10), e2306350.
(23) Shiel, H.; Hutter, O. S.; Phillips, L. J.; Swallow, J. E. N.; Jones, L. A. H.; Featherstone, T. J.; Smiles, M. J.; Thakur, P. K.; Lee, T.-L.; Dhanak, V. R.; Major, J. D.; Veal, T. D. Natural Band Alignments and Band Offsets of Sb2se3 Solar Cells. *ACS Appl. Energy Mater.* **2020**, *3* (12), 11617−11626.
(24) Sang, H.; Wang, W.; Wang, Z.; Hong, M.; Zhang, C.; Xie, S.; Ge, H.; Yan, F.; Wang, Z.; Ouyang, Y.; Liu, Y.; Wu, J.; Liu, W.; Tang, X. Tailoring Interfacial Charge Transfer for Optimizing Thermoelectric Performances of Mnte-Sb2te3 Superlattice-Like Films. *Adv. Funct. Mater.* **2022**, *33*, 2210213 DOI: 10.1002/adfm.202210213.
(25) Pant, N.; Lee, W.; Sanders, N.; Kioupakis, E. Increasing the Mobility and Power-Electronics Figure of Merit of Algan with Atomically Thin Aln/Gan Digital-Alloy Superlattices. *Appl. Phys. Lett.* **2022**, *121* (3), No. 032105, DOI: 10.1063/5.0097963.
(26) Ning, X.; Dong, Y.; Jian, W.; Wang, J.; Guo, W.; Wang, S. Record High Power Factor and Low Thermal Conductivity in Amorphous/Pbte/Amorphous Multiple Quantum Wells. *Adv. Funct. Mater.* **2023**, *33*, 2303981 DOI: 10.1002/adfm.202303981.
(27) Hori, Y.; Yatabe, Z.; Hashizume, T. Characterization of Interface States in Al2o3/Algan/Gan Structures for Improved Performance of High-Electron-Mobility Transistors. *J. Appl. Phys.* **2013**, *114* (24), No. 244503, DOI: 10.1063/1.4859576.
(28) Naithani, H.; Dasgupta, T. Critical Analysis of Single Band Modeling of Thermoelectric Materials. *ACS Appl. Energy Mater.* **2020**, *3* (3), 2200−2213.
(29) Zhu, J.; Zhang, X.; Guo, M.; Li, J.; Hu, J.; Cai, S.; Cai, W.; Zhang, Y.; Sui, J. Restructured Single Parabolic Band Model for Quick Analysis in Thermoelectricity. *npj Comput. Mater.* **2021**, *7* (1), 116 DOI: 10.1038/s41524-021-00587-5.
(30) Chen, J.; Chen, H.; Hao, F.; Ke, X.; Chen, N.; Yajima, T.; Jiang, Y.; Shi, X.; Zhou, K.; Döbeli, M.; Zhang, T.; Ge, B.; Dong, H.; Zeng, H.; Wu, W.; Chen, L. Ultrahigh Thermoelectric Performance in Srnb0. 2ti0. 8o3 Oxide Films at a Submicrometer-Scale Thickness. *ACS Energy Lett.* **2017**, *2* (4), 915−921.
(31) Li, S.; Zhao, W.; Cheng, Y.; Chen, L.; Xu, M.; Guo, K.; Pan, F. Thermoelectric Performance Enhancement in Commercial Bi(0.5)-Sb(1.5)Te(3) Materials by Introducing Gradient Cu-Doped Grain Boundaries. *ACS Appl. Mater. Interfaces* **2022**, *15*, 1167 DOI: 10.1021/acsami.2c18575.
(32) Zhao, L.; Islam, S. M. K. N.; Wang, J.; Cortie, D. L.; Wang, X.; Cheng, Z.; Wang, J.; Ye, N.; Dou, S.; Shi, X.; Chen, L.; Snyder, G. J.; Wang, X. Significant Enhancement of Figure-of-Merit in Carbon-Reinforced Cu2se Nanocrystalline Solids. *Nano Energy* **2017**, *41*, 164−171.
(33) Wei, M.; Shi, X.-L.; Zheng, Z.-H.; Li, F.; Liu, W.-D.; Xiang, L.-P.; Xie, Y.-S.; Chen, Y.-X.; Duan, J.-Y.; Ma, H.-L.; Liang, G.-X.; Zhang, X.-H.; Fan, P.; Chen, Z.-G. Directional Thermal Diffusion Realizing Inorganic Sb2te3/Te Hybrid Thin Films with High Thermoelectric Performance and Flexibility. *Adv. Funct. Mater.* **2022**, *32* (45), 2207903 DOI: 10.1002/adfm.202207903.
(34) Ahmad, M.; Agarwal, K.; Munoz, S. G.; Ghosh, A.; Kodan, N.; Kolosov, O. V.; Mehta, B. R. Engineering Interfacial Effects in Electron and Phonon Transport of Sb2te3/Mos2Multilayer for Thermoelectric Zt above 2.0. *Adv. Funct. Mater.* **2022**, *32*, 2206384 DOI: 10.1002/adfm.202206384.
(35) An, D.; Chen, S.; Lu, Z.; Li, R.; Chen, W.; Fan, W.; Wang, W.; Wu, Y. Low Thermal Conductivity and Optimized Thermoelectric Properties of P-Type Te-Sb(2)Se(3): Synergistic Effect of Doping and Defect Engineering. *ACS Appl. Mater. Interfaces* **2019**, *11* (31), 27788−27797.
(36) Wang, X. Y.; Wang, H. J.; Xiang, B.; Fu, L. W.; Zhu, H.; Chai, D.; Zhu, B.; Yu, Y.; Gao, N.; Huang, Z. Y.; Zu, F. Q. Thermoelectric Performance of Sb(2)Te(3)-Based Alloys Is Improved by Introducing Pn Junctions. *ACS Appl. Mater. Interfaces* **2018**, *10* (27), 23277−23284.
(37) Liu, X.; Zhang, B.; Chen, Y.; Wu, H.; Wang, H.; Yang, M.; Wang, G.; Xu, J.; Zhou, X.; Han, G. Achieving Enhanced Thermoelectric Performance in (Snte)(1-X)(Sb(2)Te(3))(X) and (Snte)(1-Y)(Sb(2)Se(3))(Y) Synthesized Via Solvothermal Reaction and Sintering. *ACS Appl. Mater. Interfaces* **2020**, *12* (40), 44805−44814.
(38) Siemens, M. E.; Li, Q.; Yang, R.; Nelson, K. A.; Anderson, E. H.; Murnane, M. M.; Kapteyn, H. C. Quasi-Ballistic Thermal Transport from Nanoscale Interfaces Observed Using Ultrafast Coherent Soft X-Ray Beams. *Nat. Mater.* **2010**, *9* (1), 26−30.
(39) DeCoster, M. E.; Chen, X.; Zhang, K.; Rost, C. M.; Hoglund, E. R.; Howe, J. M.; Beechem, T. E.; Baumgart, H.; Hopkins, P. E. Thermal Conductivity and Phonon Scattering Processes of Ald Grown Pbte-Pbse Thermoelectric Thin Films. *Adv. Funct. Mater.* **2019**, *29* (46), 1904073 DOI: 10.1002/adfm.201904073.
(40) Wang, Z.; Alaniz, J. E.; Jang, W.; Garay, J. E.; Dames, C. Thermal Conductivity of Nanocrystalline Silicon: Importance of Grain Size and Frequency-Dependent Mean Free Paths. *Nano Lett.* **2011**, *11* (6), 2206−2213.
(41) Zhao, Y.; Cai, Y.; Zhang, L.; Li, B.; Zhang, G.; Thong, J. T. L. Thermal Transport in 2d Semiconductors—Considerations for Device Applications. *Adv. Funct. Mater.* **2019**, *30* (8), 1903929 DOI: 10.1002/adfm.201903929.
(42) Hicks, L. D.; Dresselhaus, M. S. Effect of Quantum-Well Structures on the Thermoelectric Figure of Merit. *Phys. Rev. B* **1993**, *47* (19), 12727.

(43) Park, N. W.; Lee, W. Y.; Yoon, Y. S.; Ahn, J. Y.; Lee, J. H.; Kim, G. S.; Kim, T. G.; Choi, C. J.; Park, J. S.; Saitoh, E.; Lee, S. K. Direct Probing of Cross-Plane Thermal Properties of Atomic Layer Deposition Al(2)O(3)/Zno Superlattice Films with an Improved Figure of Merit and Their Cross-Plane Thermoelectric Generating Performance. *ACS Appl. Mater. Interfaces* **2018**, *10* (51), 44472−44482.
(44) Kieffer, J.; Valls, V.; Blanc, N.; Hennig, C. New Tools for Calibrating Diffraction Setups. *Journal of synchrotron radiation* **2020**, *27* (2), 558−566.
(45) Linseis, V.; Völklein, F.; Reith, H.; Woias, P.; Nielsch, K. Platform for in-Planeztmeasurement and Hall Coefficient Determination of Thin Films in a Temperature Range from 120 K up to 450 K. *J. Mater. Res.* **2016**, *31* (20), 3196−3204.
(46) Linseis, V.; Volklein, F.; Reith, H.; Nielsch, K.; Woias, P. Advanced Platform for the in-Plane Zt Measurement of Thin Films. *Rev. Sci. Instrum.* **2018**, *89* (1), No. 015110.
(47) Perdew, J. P.; Burke, K.; Ernzerhof, M. Generalized Gradient Approximation Made Simple. *Phys. Rev. Lett.* **1996**, *77* (18), 3865.
(48) Blum, V.; Gehrke, R.; Hanke, F.; Havu, P.; Havu, V.; Ren, X.; Reuter, K.; Scheffler, M. Ab Initio Molecular Simulations with Numeric Atom-Centered Orbitals. *Comput. Phys. Commun.* **2009**, *180* (11), 2175−2196.
(49) Krukau, A. V.; Vydrov, O. A.; Izmaylov, A. F.; Scuseria, G. E. Influence of the Exchange Screening Parameter on the Performance of Screened Hybrid Functionals. *J. Chem. Phys.* **2006**, *125* (22), No. 224106, DOI: 10.1063/1.2404663.
(50) Boubekraoui, A.; Moatassim, H.; Al-Shami, A.; Ez-Zahraouy, H. Dft Study of Structural, Electronic, and Thermoelectric Properties of Cs2pdx (X= Br2be2te2) Compound. *Computational Condensed Matter* **2021**, *29*, No. e00600.
(51) Solola, G. T.; Klopov, M.; Akinami, J. O.; Afolabi, T. A.; Karazhanov, S. Z.; Adebayo, G. First Principle Calculations of Structural, Electronic, Optical and Thermoelectric Properties of Tin (Ii) Oxide. *Materials Research Express* **2019**, *6* (12), No. 125915.
(52) Hermann, J.; Tkatchenko, A. Density Functional Model for Van Der Waals Interactions: Unifying Many-Body Atomic Approaches with Nonlocal Functionals. *Phys. Rev. Lett.* **2020**, *124* (14), No. 146401.
(53) Huhn, W. P.; Blum, V. One-Hundred-Three Compound Band-Structure Benchmark of Post-Self-Consistent Spin-Orbit Coupling Treatments in Density Functional Theory. *Physical Review Materials* **2017**, *1* (3), No. 033803.
(54) Madsen, G. K. H.; Carrete, J.; Verstraete, M. J. Boltztrap2, a Program for Interpolating Band Structures and Calculating Semi-Classical Transport Coefficients. *Comput. Phys. Commun.* **2018**, *231*, 140−145.
(55) Alvarez, D. Juwels Cluster and Booster: Exascale Pathfinder with Modular Supercomputing Architecture at Juelich Supercomputing Centre. *Journal of large-scale research facilities JLSRF* **2021**, *7*, A183−A183.

https://doi.org/10.1021/acsnano.3c13152
ACS Nano 2024, 18, 17500−17508